Science Advances

AAAS

advances.sciencemag.org/cgi/content/full/4/1/eaao5747/DC1

Supplementary Materials for

Disequilibrium biosignatures over Earth history and implications for detecting exoplanet life

Joshua Krissansen-Totton, Stephanie Olson, David C. Catling

Published 24 January 2018, *Sci. Adv.* **4**, eaao5747 (2018)
DOI: 10.1126/sciadv.aao5747

This PDF file includes:

Supplementary Materials

Supplementary Text

section S1. The omission of solids, redox-sensitive nonvolatile aqueous species, and ocean heterogeneity

We neglected redox-sensitive, non-volatile aqueous species because they are not remotely observable, but this omission does not affect our results significantly. The most abundant redox-sensitive, non-volatile aqueous species in the Precambrian ocean was iron. If the Precambrian ocean was mostly ferruginous, then aqueous Fe^{2+} could react with O_2 or with aqueous NO_3^- derived from N_2 oxidation (92), thereby adding to the maximum Proterozoic available energy. To test this, we repeated maximum Proterozoic disequilibrium calculations using Aspen Plus and varied the concentration of ferrous iron (with zero initial ferric iron). If Fe^{2+} concentrations in the Precambrian oceans were 7×10^{-5} mol/kg (5.5×10^{-4} mol per mol of atmosphere), assuming siderite saturation (93), then only ~13 J/mol are added from Fe^{2+} oxidation, a 2% increase from the nominal maximum Proterozoic case. Even if Fe^{2+} concentrations were extremely high due to siderite supersaturation (94), for instance 3×10^{-3} mol/kg (0.023 mol per mol of atmosphere), then the available energy is 1197 J/mol. This is still less than the Phanerozoic disequilibrium, and does not change the qualitative disequilibrium evolution in Fig. 2.

By assuming saturation to obtain initial dissolved gas abundances, we are neglecting the possible contribution from ocean heterogeneity. Specifically, by adopting Henry's law to calculate the initial dissolved oxygen abundance, we may be overestimating the Proterozoic disequilibrium because the Proterozoic ocean was mostly anoxic. However, even at saturation, the number of moles of oxygen in the ocean is about two orders of magnitude less than the atmosphere, and so the total available energy will be overestimated only very slightly. If the maximum Proterozoic disequilibrium calculation is repeated with zero dissolved oxygen in the initial state, then the total available energy is only 6 J/mol lower than when oxygen saturation is assumed (<1% difference). This calculation also shows that oxygen oases in the Archean (95) and Proterozoic (96) will have a negligible effect on the global disequilibrium – a realistic Precambrian ocean with 1-10% oxic waters will yield an available energy somewhere between our O_2-saturated nominal calculation, and the zero dissolved oxygen endmembers. However, oxygen oases still represent an important example of local disequilibria maintained by life that would be very difficult to detect remotely.

section S2. Full results and Aspen Plus validation

Tables S1, S2, S3, S4, and S5 show full multiphase equilibrium results for our Proterozoic maximum, Proterozoic minimum, Proterozoic mid-level oxygen, Archean maximum, and Archean minimum scenarios, respectively.

section S3. Reactions associated with Precambrian disequilibria and their Gibbs energy contributions

Table S6 shows the various reactions contributing to Proterozoic disequilibrium, and the Gibbs energy contribution from each of these reactions. Since methane levels were potentially high in the Proterozoic, the contribution from methane oxidation (75 J/mol) to the maximum Proterozoic disequilibrium is much higher than the ~1.3 J/mol contribution to the modern Earth. Contributions from the oxidation of aqueous species such as ammonium and sulfide only contribute 14% to the total available Gibbs energy (maximum case), and are not relevant for life detection on exoplanets since changes in ocean speciation are not remotely observable.

Table S7 shows the various reactions contributing to Archean disequilibrium, and the Gibbs energy contribution from each of these reactions. The second largest contributor to maximum Archean disequilibrium (after ammonium formation from methane oxidation) is the oxidation of carbon monoxide.

section S4. Sensitivity of available Gibbs energy to difficult-to-observe variables

Table S8 shows the thermodynamic disequilibrium for our maximum Archean case where we have varied parameters such as temperature, ocean pH/alkalinity, ocean salinity, ocean volume, atmospheric pressure, and atmospheric bulk composition. Theses variables are challenging to observe for exoplanets, and so this table explores whether it would be possible to quantify the presence of thermodynamic disequilibrium for an Archean-like exoplanet. Results are reported for both Matlab and ASPEN calculations, and the two computational methods agree to within a few percent in every case, validating our Matlab calculations.

The CH_4-depleting reaction went to completion (i.e. all CH_4 was used up in a forward reaction) regardless of temperature.

Ocean alkalinity was varied by solving the carbonate system equilibria for a system with pCO_2 = 0.5 bar and the specified alkalinity from the table S8 (25). Next, Na(+) abundances were adjusted from their nominal values to maintain charge balance. We find that for the high alkalinity case (200 mmol/kg) the CH_4-depleting reaction only depletes 89% of the methane in equilibrium, as opposed to over 99% in other sensitivity tests. This case is highlighted in bold in table S8. However, alkalinities this high are unlikely to occur given buffering from silicate weathering (29).

Ocean salinity was varied by increasing (or decreasing) Na(+) and Cl(-) by the same amount, thereby preserving carbonate alkalinity. The CH_4-depleting reaction went to completion regardless of salinity.

Ocean volume was varied by scaling the liquid water abundances and other aqueous constituents by the specified amount. All reactions went to completion except the very low ocean volume case, which is highlighted in bold in table S8. Note that in the extreme case of no ocean, reaction (4) does not occur and the Archean disequilibrium is small (Fig. 2) and is dominated by CO oxidation (table S7). Promising strategies for constraining ocean volume remotely such as glint,

polarization, time-resolved photometry, geophysical theory, and thermal inertia, are discussed in Krissansen-Totton *et al.* (25). However, even if surface oceans cannot be directly detected, for instance because of haze obscuring surface features, then it may still be possible to infer the presence of an ocean. If water vapor abundance at a particular pressure level can be constrained, then climate models could be applied to check for consistency with a steam atmosphere.

Archean total pressure may have been less than 1 bar (97-99), and exoplanet surface pressures may vary considerably, and so we also calculate the sensitivity of our disequilibrium to total atmospheric pressure. Atmospheric pressure was varied by changing the gas-phase pressure and adjusting the liquid-to-gas ratio by the inverse amount. This accounts for Archean pressure being lower (higher) because of fewer (more) moles in the atmosphere, not because of a change in gravity. The carbonate equilibria was solved for the new initial conditions, and Na(+) abundances were adjusted to preserve charge balance. For the more extreme cases, the initial water phase separation needed to be readjusted using Henry's law (see methods). The CH_4-depleting reaction went to completion regardless of pressure, and for modest changes in pressure (0.5 bar or 2 bar), the available Gibbs energy is very similar to the 1 bar case.

Finally, we considered lower pressure in conjunction with different bulk abundances. This is relevant to the early Archean where there is considerable uncertainty in atmospheric composition. The maximum Archean disequilibrium was calculated for both 17 % N_2 with 80% CO_2, and for 77% N_2 with 20% CO_2 (the remaining 3% is water vapor and CH_4 as shown in table S4). The available energy in these cases is very similar to the nominal case (47% CO_2 and 50% N_2). Even with only 2% N_2 abundance and 95% CO_2 abundance (at 1 bar), the available energy is still comparable to the nominal case. These results imply that it is not necessary to constrain the N_2 abundance precisely in order to calculate thermodynamic disequilibrium. So long as there is enough N_2 to oxidize all the CH_4, reaction (4) will go to completion and the available energy will be large.

section S5. Abiotic CH_4 formation from high-temperature processes

Abiotic CH_4 outgassed from a highly reduced mantle would be easily distinguishable from biotic methane. The thermodynamic calculations reported here are derived in Catling and Kasting (26, Ch. 7). For temperature-pressure conditions relevant to surface volcanism (T = 1200 °C, P = 5 atm) and Earth-like oxygen fugacity for the upper mantle (near the quartz-fayalite-magnetite buffer, $f_{O_2} = 10^{-8.5}$ bar), the predicted CH_4/CO_2 ratio of magmatic gases in thermodynamic equilibrium is 9.4×10^{-11}. This result explains why negligible CH_4 is outgassed from volcanoes on the modern Earth (100), except from the thermal decomposition of organic matter.

Let us consider scenarios that might make volcanic CH_4 non-negligible. If the mantle oxygen fugacity is four orders of magnitude lower than Earth's upper-mantle, comparable to inferences from some Mars meteorites (101), then the predicted CH_4/CO_2 ratio is ~0.01. The CO_2 outgassing flux on the modern Earth is around 10 Tmol/yr (102), and so even in this extreme case the predicted methane flux is only 0.1 Tmol/yr. However, if the total outgassing flux was 1-2 orders of magnitude higher, as is possible for the early Earth, then the volcanic methane flux could extend into the Tmol/yr range, comparable to the modern biological flux. Yet in this scenario, the predicted CO/CH_4 ratio is ~6. The atmosphere of such a planet would be rich in

CO. Because CO has many readily observable spectral features (42), this planet would be easily distinguished from a CO_2-CH_4 biosignature. The coexistence of atmospheric carbon at opposite ends of the redox spectrum (+4 in CO_2 and -4 in CH_4) with no intermediate (+2) CO cannot be explained by high-temperature outgassing alone.

Other high temperature processes have been proposed for abiotic CH_4 such as iron carbonate decomposition, graphite metamorphism, clay-catalyzed hydrocarbon synthesis, and organosulfur reactions (41,103). These pathways are either unlikely to be significant on a global scale, have not been well quantified, or in the case of graphite, are likely ultimately sourced from organic carbon.

section S6. Atmospheric kinetics of methane destruction

Figure S3 shows how surface methane fluxes are related to steady state methane abundances for anoxic atmospheres. The solid black line is from Kasting and Brown (77) where a Sun-like star is assumed and a photochemical model is used to compute steady state CH_4 abundances in Earth's early atmosphere. The relationship looks similar for an Archean-Earth-like exoplanet atmosphere around M-dwarfs because the dominant sink for atmospheric methane in anoxic atmospheres is photochemical destruction and hydrogen escape (104). In steady state, the net H source to the anoxic atmosphere will be balanced by the net loss of H via escape at the top of the atmosphere

$$F_{escape} = F_{input} \text{ (of H atoms)} \quad \text{(S1)}$$

If we assume the H input source is primarily the CH_4 flux into the atmosphere, as is likely for planets with large biological CH_4 fluxes (59), and that H escape is diffusion limited, then equation (S1) becomes

$$k_{esc} f_{tot} = 4F_{CH_4} \quad \text{(S2)}$$

where k_{esc} =2.5×10^{13} cm^{-2} s^{-1} is from diffusion-limited escape theory (see below), F_{CH_4} is the CH_4 flux to the atmosphere (Tmol CH_4/yr), and we weight CH_4 fluxes by the number of H atoms per molecule.

Because of efficient turbulent mixing below the homopause, the total hydrogen mixing ratio at the homopause is the same as that immediately above the troposphere and dominated by CH_4, so

$$f_{tot} \approx 4 f_{CH_4} \quad \text{(S3)}$$

Where f_{CH_4} is the CH_4 mixing ratio. Thus by combining equations (S2) and (S3) and rearranging with a conversion factor to global Teramole (10^{12} mole) fluxes of CH_4, we have

$$f_{\mathrm{CH_4}} = F_{\mathrm{CH_4}} / k_{esc} = F_{\mathrm{CH_4}}\ (\mathrm{Tmol/yr}) / 6680\ (\mathrm{Tmol/yr}) \quad \text{(S4)}$$

The constant $k_{esc} = b(T) / H_a(T)$, where $b(T)$ is a binary diffusion coefficient weakly dependent on the temperature at the homopause and $H_a(T)$ is the temperature-dependent scale height at the homopause (see (26) for details). Here, we assume $b(T = 208\ \mathrm{K}) / H_a(T = 208\ \mathrm{K}) = 2.5\times10^{13}$ molecules cm^{-1} s^{-1} = 6680 Tmol/yr.

In fig. S3 we plot the steady state abundances derived from this diffusion-limited escape rate for homopause temperatures of T=150 K, 200 K, and 250 K, and an Earth-like scale-height (corrected for temperature). These lines provide a lower limit on CH_4 fluxes for any given CH_4 abundance. For instance, if there are other H-bearing gases (e.g. high H_2), then $f_{tot} > 4 f_{CH_4}$ and the actual CH_4 flux required to maintain an observed CH_4 abundance may be higher than the diffusion limit suggests (note that a change in this direction would only strengthen the case for biology). For planets with different atmospheric bulk abundances (e.g. CO_2-dominated) or different surface gravities, the homopause scale height will change and so the diffusion limit will be slightly shifted relative to the lines plotted in fig. S3.

In principle, the diffusion limit is independent of stellar type, and so the linear relationship between fluxes and abundances in fig. S17 is expected to apply to all habitable exoplanets with anoxic atmospheres. Escape rates slower than the diffusion limit are unlikely because even for cold thermospheres, non-thermal escape process compensate for lowered Jeans' escape (68). Photodissociation of CH_4 and therefore the rate of hydrogen escape is ultimately limited by the shortwave (<145 nm) stellar flux. The dominant stellar flux at these wavelengths comes from the Lyman-α line (121.6 nm), and habitable zone planets around M stars typically receive higher Lyman-α fluxes than habitable zones planets around G stars (105). We therefore expect hydrogen escape around M stars to be limited by diffusion, and not by CH_4 photodissociation.

Figure S3 suggests that CH_4 abundances in excess of 1.5×10^{-3} imply surface fluxes in excess of 10 Tmol CH_4/yr, which is likely biological (Fig. 6), whereas CH_4 abundances in excess of 10^{-2} imply surface fluxes in excess of 50 Tmol CH_4/yr, which is very likely biological (Fig. 6). Today's flux of CH_4 to the Earth's atmosphere is ~30 Tmol CH_4/yr, for comparison.

Naturally, the calculations outlined above are to be interpreted as approximations. If methane is observed on a nearby exoplanet, then photochemical modeling using the observed stellar spectrum might be attempted to produce a more precise version of fig. S3. Once CH_4 abundances have been constrained by observation, the corresponding escape flux, and by extension the surface source flux can be inferred. This can then be compared to the likely distribution of maximum abiotic source fluxes.

Supplementary figures and tables

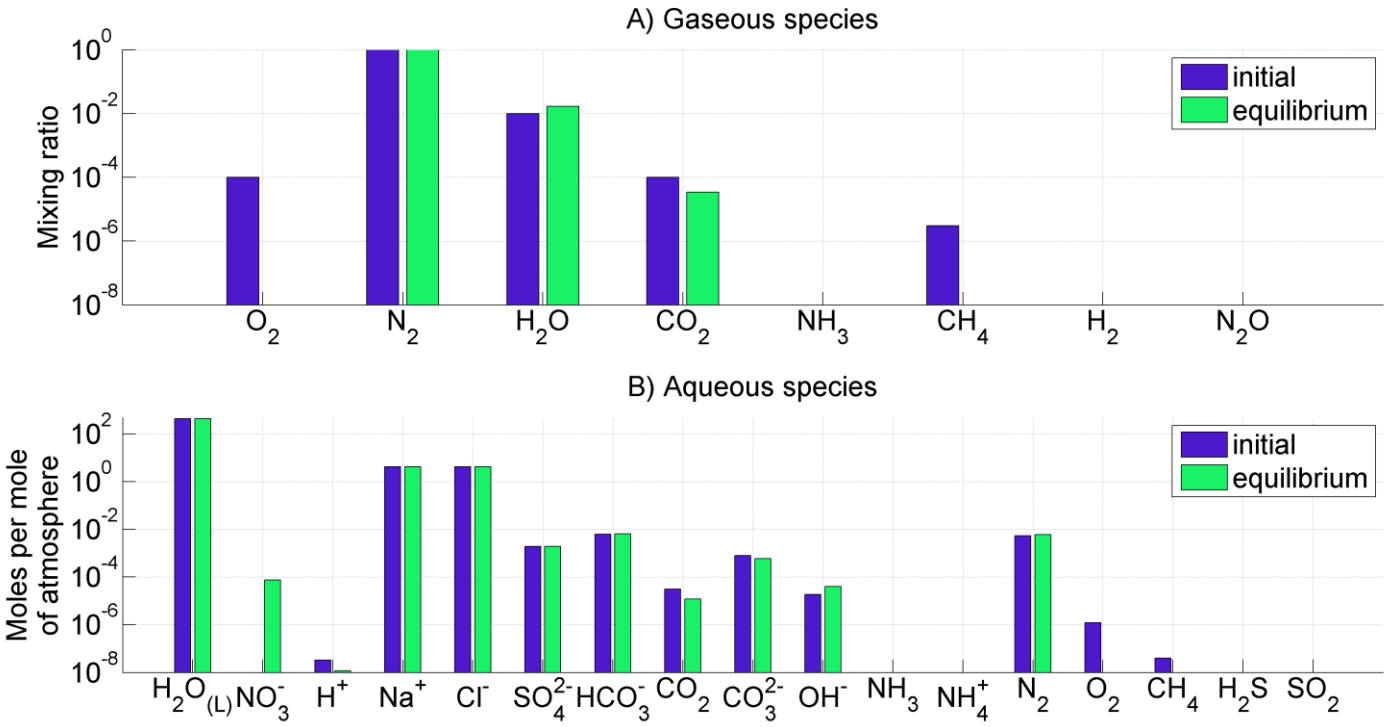

fig. S1. Atmosphere-ocean disequilibrium in the Proterozoic (minimum disequilibrium scenario). Blue bars denote assumed initial abundances from the literature, and green bars denote equilibrium abundances calculated using Gibbs free energy minimization. Subplots separate (**A**) atmospheric species and (**B**) ocean species.

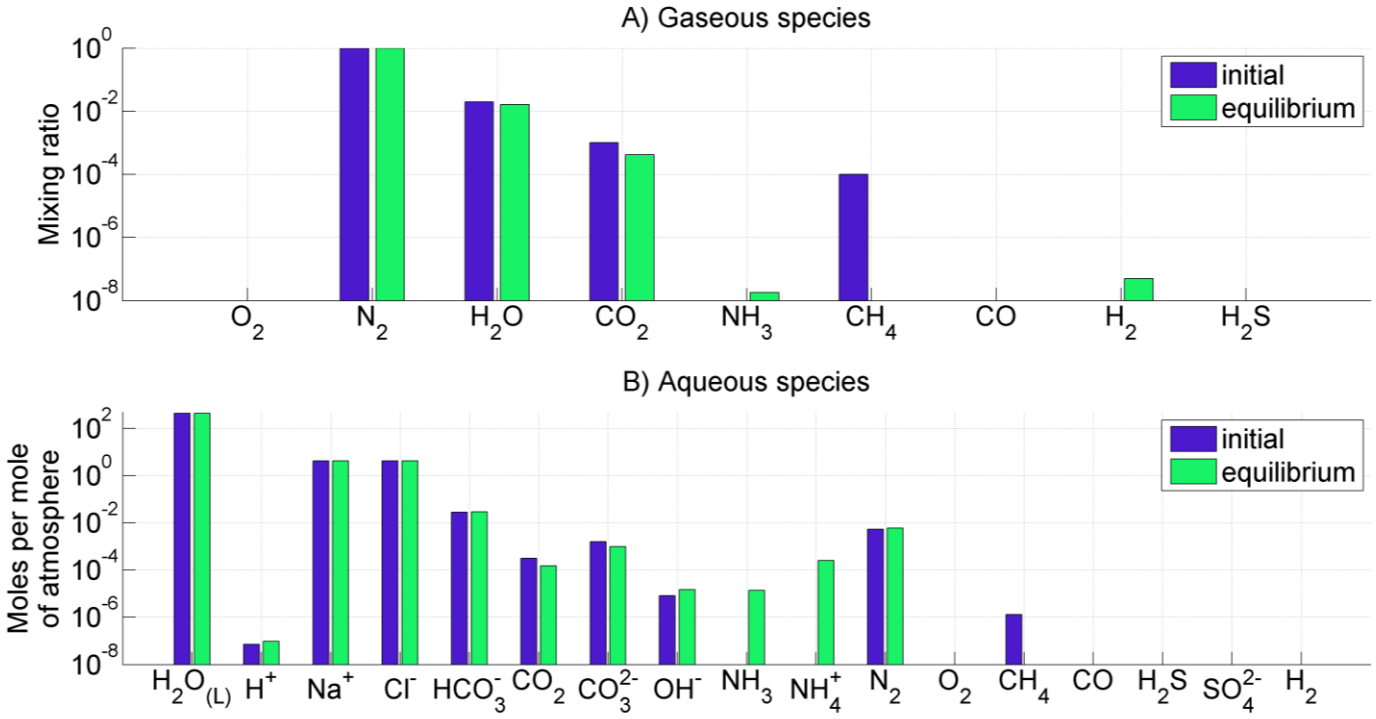

fig. S2. Atmosphere-ocean disequilibrium in the Archean (minimum disequilibrium scenario). Blue bars denote assumed initial abundances from the literature, and green bars denote equilibrium abundances calculated using Gibbs free energy minimization. Subplots separate (**A**) atmospheric species and (**B**) ocean species. Note that even in the minimum disequilibrium case, atmospheric CH_4 is depleted by reaction to equilibrium.

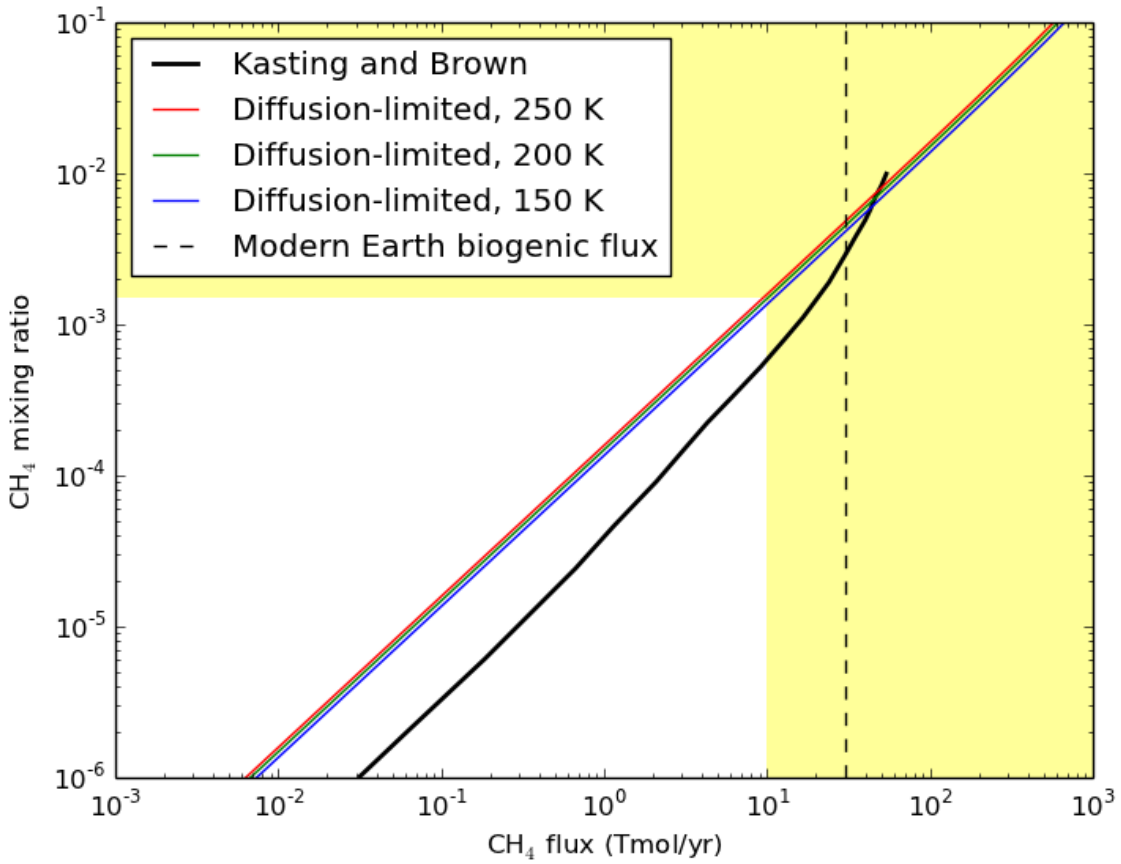

fig. S3. Relationship between methane fluxes and atmospheric abundances. The black line is derived in (77) using a photochemical model for the early Earth's atmosphere, assuming a Sun-like star. The red, green, and blue lines are derived assuming diffusion-limited escape of hydrogen with homopause temperatures of 250 K, 200 K, and 150 K, respectively. Diffusion-limited escape demarcates the minimum methane flux required to sustain any given methane abundance. Note that the diffusion-limited escape model may overestimate the CH_4 mixing ratio at any given flux by a factor of 2-3 because it does not account for other CH_4 sinks.

table S1. Proterozoic maximum disequilibrium. Mixing ratios are reported for gaseous species, and moles per mole of atmosphere for aqueous species. Note that final Aspen values that do not completely conserve mass and charge are an artifact of Aspen automatically adjusting initial abundances slightly before performing Gibbs energy calculations.

	Initial	Matlab final	Aspen final
H_2O(liquid)	436.788155	436.793984	436.7938
O_2	0.03	2.64E-05	5.59E-05
N_2	0.86	0.84759313	0.8485178
H_2O	0.01	0.01627808	0.0163399
CO_2	0.1	0.11308654	0.1148073
NH_3	1.00E-15	3.47E-12	0
CH_4	0.0001	1.29E-12	0
H_2	2.00E-06	5.32E-12	0
N_2O	1.00E-06	1.47E-11	0
NO_3(-)	7.83E-15	0.02387899	0.0238104
H(+)	8.74E-06	0.001014	0.00119341
Na(+)	4.3773073	4.3773073	4.338146
Cl(-)	4.27587006	4.27587006	4.237616
SO_4(2-)	0.03916493	0.03916493	0.0388458
HCO_3(-)	0.02348567	0.00024239	0.000221296
CO_2(aq)	0.03135339	0.04162247	0.0397126
CO_3(2-)	1.10E-05	9.20E-10	3.38E-10
OH(-)	7.02E-08	1.00E-15	4.13E-10
NH_3(aq)	7.79E-13	3.89E-12	0
NH_4(+)	0.00039165	4.61E-12	0
N_2(aq)	0.00470212	0.00536632	0.0044815
O_2(aq)	0.00037233	3.37E-07	5.91E-07
CH_4(aq)	1.32E-06	1.28E-12	0
H_2S(aq)	1.00E-15	1.52E-12	0
SO_2(aq)	7.83E-15	4.58E-12	0
Available Gibbs energy, Φ (J/mol)		**884**	**860**

table S2. Proterozoic minimum disequilibrium. Mixing ratios are reported for gaseous species, and moles per mole of atmosphere for aqueous species. Note that final Aspen values that do not completely conserve mass and charge are an artifact of Aspen automatically adjusting initial abundances slightly before performing Gibbs energy calculations.

	Initial	Matlab final	Aspen final
H_2O(liquid)	436.7881549	436.7814412	436.7812
O_2	0.0001	2.64E-12	0
N_2	0.99	0.989253694	0.9894527
H_2O	0.01	0.01657188	0.0167461
CO_2	0.0001	3.39E-05	1.25128E-05
NH_3	1.00E-15	4.09E-12	0
CH_4	3.00E-06	1.44E-12	0
H_2	1.00E-15	1.45E-11	0
N_2O	1.00E-15	1.33E-11	0
NO_3(-)	7.83E-15	7.61E-05	7.61295E-05
H(+)	3.28E-08	1.20E-08	1.56172E-08
Na(+)	4.287638267	4.287638267	4.28568
Cl(-)	4.275870063	4.275870063	4.273917
SO_4(2-)	0.001958246	0.001958246	0.00195735
HCO_3(-)	0.006265174	0.00653947	0.00658799
CO_2(aq)	3.14E-05	1.21E-05	4.57563E-06
CO_3(2-)	7.84E-04	5.98E-04	5.75E-04
OH(-)	1.87E-05	4.02E-05	3.36E-05
NH_3(aq)	7.79E-13	4.40E-12	0
NH_4(+)	7.83E-15	4.62E-12	0
N_2(aq)	0.005412906	0.006121147	0.00592217
O_2(aq)	1.24E-06	7.42E-11	0
CH_4(aq)	3.96E-08	1.42E-12	0
H_2S(aq)	7.83E-15	1.46E-12	0
SO_2(aq)	7.83E-15	4.08E-12	0
Available Gibbs energy, Φ (J/mol)		**9.54**	**9.26**

table S3. Proterozoic disequilibrium with 2% PAL of O_2. Mixing ratios are reported for gaseous species, and moles per mole of atmosphere for aqueous species. The available energy from this scenario separates the lightly and darkly shaded region in Fig. 2. Note that final Aspen values that do not completely conserve mass and charge are an artifact of Aspen automatically adjusting initial abundances slightly before performing Gibbs energy calculations.

	Initial	final matlab	final - ASPEN
H_2O(liquid)	436.7882	436.7825	436.7822
O_2	0.004	1.00E-15	3.55854E-08
N_2	0.985897	0.983636	0.9887316
H_2O	0.01	0.016433	0.0167926
CO_2	0.0001	0.001867	0.0019125
NH_3	1.00E-15	7.77E-13	0
CH_4	3.00E-06	5.83E-14	0
H_2	1.00E-15	1.27E-12	0
N_2O	1.00E-15	3.27E-12	0
NO_3(-)	7.83E-15	0.003196	0.0031961
H(+)	3.28E-08	8.36E-07	9.05431E-07
Na(+)	4.287638	4.287638	4.28568
Cl(-)	4.27587	4.27587	4.273917
SO_4(2-)	0.001958	0.001958	0.00195735
HCO_3(-)	0.006265	0.004645	0.00463422
CO_2(aq)	3.14E-05	0.000666	0.000624464
CO_3(2-)	7.84E-04	5.57E-06	9.08882E-06
OH(-)	1.87E-05	5.25E-07	5.30271E-07
NH_3(aq)	7.79E-13	8.48E-13	0
NH_4(+)	7.83E-15	9.07E-13	0
N_2(aq)	0.005413	0.006076	0.00508327
O_2(aq)	1.24E-06	7.14E-10	3.6597E-10
CH_4(aq)	3.96E-08	2.77E-13	0
H_2S(aq)	7.83E-15	2.79E-13	0
SO_2(aq)	7.83E-15	8.60E-13	0
Available Gibbs energy, Φ (J/mol)		**135**	**128**

table S4. Archean maximum disequilibrium. Mixing ratios are reported for gaseous species, and moles per mole of atmosphere for aqueous species. Note that final Aspen values that do not completely conserve mass and charge are an artifact of Aspen automatically adjusting initial abundances slightly before performing Gibbs energy calculations.

	Initial	final matlab	final - ASPEN
H_2O(liquid)	436.77573	436.734522	436.9592
O_2	2.00E-07	1.63E-13	0
N_2	0.5	0.48682701	0.4874388
H_2O	2.00E-02	0.01591615	0.0158566
CO_2	0.47	0.44878826	0.4465212
NH_3	1.00E-09	1.59E-08	1.97E-08
CH_4	0.01	1.91E-05	3.48E-05
CO	0.001	1.00E-15	1.08E-11
H_2	0.0001	5.98E-08	7.05E-08
H_2S	3.1326E-05	0.0004157	0.00047851
H(+)	3.29E-06	3.02E-06	3.16E-06
Na(+)	4.59192496	4.59192496	4.594223
Cl(-)	4.28E+00	4.27587006	4.277862
HCO_3(-)	0.31253612	0.3402181	0.3402828
CO_2(aq)	0.16551098	0.17043556	0.172843
CO_3(2-)	0.00039017	0.00011673	0.00020317
OH(-)	1.87E-07	1.49E-07	1.60E-07
NH_3(aq)	7.79E-07	1.36E-05	1.26E-05
NH_4(+)	0.00039165	0.02585194	0.0256976
N_2(aq)	0.00273379	0.00317021	0.00263621
O_2(aq)	2.03E-09	1.31E-14	0
CH_4(aq)	0.00013211	3.01E-07	4.21E-07
CO(aq)	8.66E-06	1.24E-12	8.62E-14
H_2S(aq)	3.13E-05	0.00048445	0.00046404
SO_4(2-)	0.0015666	0.00072908	0.00068588
H_2(aq)	6.48E-07	3.28E-11	4.19E-10
Available Gibbs energy, Φ (J/mol)		**234**	**232**

table S5. Archean minimum disequilibrium. Mixing ratios are reported for gaseous species, and moles per mole of atmosphere for aqueous species. Note that final Aspen values that do not completely conserve mass and charge are an artifact of Aspen automatically adjusting initial abundances slightly before performing Gibbs energy calculations.

	initial	final matlab	final - ASPEN
H_2O(liquid)	436.77573	436.778199	437.0025
O_2	1.00E-15	5.17E-13	0
N_2	0.98	0.979146	0.9801331
H_2O	2.00E-02	0.01647763	0.0166226
CO_2	0.001	0.00042043	0.00057407
NH_3	1.00E-15	1.80E-08	1.51E-08
CH_4	0.0001	9.40E-09	7.91E-09
CO	1.00E-15	8.58E-12	0
H_2	1.00E-15	5.03E-08	4.85E-08
H_2S	7.83E-15	7.83E-15	0
H(+)	7.29E-08	9.70E-08	4.38E-08
Na(+)	4.30721038	4.30721038	4.30721
Cl(-)	4.28E+00	4.27587006	4.27587
HCO_3(-)	0.02816377	0.02960221	0.0292059
CO_2(aq)	0.00031353	0.00015015	0.00019063
CO_3(2-)	0.00158412	9.90E-04	0.00119208
OH(-)	8.38E-06	1.47E-05	1.10E-05
NH_3(aq)	7.83E-15	1.37E-05	9.33E-06
NH_4(+)	7.83E-15	0.00025639	0.00026079
N_2(aq)	0.00535822	6.08E-03	0.00509003
O_2(aq)	1.00E-15	5.01E-13	0
CH_4(aq)	1.32E-06	9.88E-11	9.18E-11
CO(aq)	1.00E-15	5.73E-12	0
H_2S(aq)	7.83E-15	7.83E-15	0
SO_4(2-)	7.83E-15	7.83E-15	0
H_2(aq)	1.00E-15	2.21E-10	2.77E-10
Available Gibbs energy, Φ (J/mol)		**5.1**	**3.4**

table S6. Reactions contributing to Proterozoic disequilibrium. Note that the contributing Gibbs energies do not sum exactly to the total available energy because there are additional contributions from water activity changes, and because reactions are not independent.

Description	Reaction	Contribution to maximum disequilibrium	Contribution to minimum disequilibrium
Nitrate formation	$5O_2 + 2N_2 + 2H_2O \rightarrow 4H^+ + 4NO_3^-$	640 J/mol (72%)	7.4 J/mol (79%)
Carbonate speciation from ocean acidification	$HCO_3^- + H^+ \rightarrow H_2O + CO_2$		
Ammonium oxidation	$3O_2 + 4NH_4^+ \rightarrow 6H_2O + 4H^+ + 2N_2$	101 J/mol (11%)	0 J/mol (0%)
Methane oxidation	$CH_4 + 2O_2 \rightarrow 2H_2O + CO_2$	75 J/mol (8%)	2.1 J/mol (23%)
Sulfide oxidation	$H_2S + 2O_2 \rightarrow 2H^+ + SO_4^{2-}$	27 J/mol (3%)	0 J/mol (0%)
Total available Gibbs energy		884 J/mol	9.5 J/mol

table S7. Reactions contributing to Archean disequilibrium. Note that the contributing Gibbs energies do not sum exactly to the total available energy because there are additional contributions from water activity changes, and because reactions are not independent. For instance, hydrogen oxidation produces methane that then adds to ammonium formation.

Description	Reaction	Contribution to maximum disequilibrium	Contribution to minimum disequilibrium
Ammonium formation	$5CO_2 + 4N_2 + 3CH_4 + 14H_2O \rightarrow 8NH_4^+ + 8HCO_3^-$	170 J/mol (74%)	4 J/mol (80%)
Carbon monoxide oxidation	$4CO + 2H_2O \rightarrow 3CO_2 + CH_4$	42 J/mol (18%)	0 J/mol (0%)
Hydrogen oxidation	$CO_2 + 4H_2 \rightarrow 2H_2O + CH_4$	2 J/mol (1%)	0 J/mol (0%)
Sulfate reduction	$CO_2 + CH_4 + SO_4^{2-} \rightarrow H_2S + 2HCO_3^-$	3 J/mol (1%)	0 J/mol (0%)
Carbon speciation	$H_2O + CO_2 + CO_3^{2-} \rightarrow 2HCO_3^-$	<1 J/mol (<1%)	1 J/mol (20%)
Ammonia formation	$N_2 + 3H_2 \rightarrow 2NH_3$	<1 J/mol (<1%)	0 J/mol (0%)
Total available Gibbs energy		231 J/mol	5.1 J/mol

table S8. Sensitivity of Archean disequilibrium to difficult-to-observe variables.
Disequilibria values highlight in bold indicate scenarios where methane-depletion did not occur (<90% depletion). Available energies are reported for both our Matlab calculations, and the commercial software package Aspen Plus, and the two methods are in agreement.

		Available Gibbs free energy (J/mol)	
		Matlab	ASPEN
Temperature, K	273.15	369	359
	288.15	234	232
	298.15	220	204
Ocean alkalinity, mmol/kg (pH)	4 (pH=5.4)	363	359
	40 (pH=6.4)	234	232
	200 (pH=7.1)	152	**181**
Ocean salinity, relative to modern	0.1	199	198
	1	234	232
	10	249	223
Ocean volume, relative to modern	0.1	**89**	**89**
	0.5	188	187
	1	234	232
	2	279	277
	10	405	401
	50	701	682
Atmospheric pressure, atm	0.1	125	141
	0.5	220	213
	1	234	232
	2	271	262
	10	366	354
Low pressure (0.5 bar) and variable bulk abundances	17% N_2, 80% CO_2	198	191
	50% N_2, 47% CO_2	220	213
	77% N_2, 20% CO_2	224	214
Low N2 abundance	2% N_2, 95% CO_2	151	150
	50% N_2, 47% CO_2	234	232